






Computational studies of the order-disorder transition in block copolymer topological blends

Rahul Kumar ¹, Amy D. Goodson,¹ Haroon Alli ¹, Clayton Chamness,¹ Isabella L. Misericocchi ^{1,2}, Henry S. Ashbaugh ¹ and Julie N. L. Albert ¹

¹Department of Chemical and Biomolecular Engineering, Tulane University, New Orleans, Louisiana 70118, USA

²Department of Chemical and Biomolecular Engineering, Lafayette College, Easton, Pennsylvania 18042, USA



(Received 15 November 2023; accepted 1 March 2024; published 10 April 2024)

Block copolymer (BCP) nanolithography provides an economical way to pattern nanoscale features for the semiconductor industry. Molecular cyclization can reduce feature sizes, but like linear BCPs, cyclic BCP nanostructure size is limited by the order-disorder transition (ODT). Although the ODTs of pure linear and cyclic BCPs have been studied extensively, there is little information on binary blends of these BCPs. Here, we use dissipative particle dynamic simulations to study the impact of size mismatch and molecular architecture of component BCPs on the ODT for various blends. We see that the blend ODT always occurs at higher segregation strength than one would predict from linear interpolation between pure-component ODTs. The deviation from this simple prediction is greater for blends with greater size mismatch between components. We find clustering of like components (i.e., linear BCPs with linear BCPs and cyclic BCPs with cyclic BCPs) in the disordered phase, and the characteristic lengths of the component clusters correlate with molecular size. Because the ordered state consists of uniformly spaced lamellae, which requires interdigitation of linear and cyclic components of the blend, resolution of the size mismatch between clusters seen in the disordered state can be thought of as a barrier to ordering.

DOI: [10.1103/PhysRevMaterials.8.045603](https://doi.org/10.1103/PhysRevMaterials.8.045603)

I. INTRODUCTION

Based on historical trends, Gordon Moore predicted in 1965 that computing power would grow exponentially with the number of transistors on a computer chip doubling every 18 months [1]. Moore's "law" was realized over the next 50 years, in large part due to advancements in photolithography techniques that enabled the fabrication of ever-smaller feature sizes. Furthermore, according to The 2017 IRDS Lithography Roadmap [2], the semiconductor industries will need sub-10-nm features by 2024 to meet the rising demands of high-performance logic devices. Photolithographic fabrication of sub-10-nm features, however, is expensive due to the extremely short-wavelength ultraviolet light source required [3] and high-resolution tools needed to overcome light's diffraction limit [4]. This cost presents a bottleneck for the continuous advancement promised by Moore's law. Block copolymers (BCPs) can form assemblies on the length scale of individual polymer chains with sub-10-nm sizes, providing a potential alternative to traditional photolithography with lower costs. Thanks to several decades of research on the fundamental principles of BCP self-assembly, several strategies for controlling nanostructure size and orientation in thin films, minimizing defects, and transferring the BCP pattern to a

semiconductor chip are available to meet the nanolithography needs of the semiconductor industry [5–8].

A linear BCP consists of two chemically distinct blocks (referred to as A and B) that are incompatible in the melt. The self-assembled structures of pure BCPs exhibit a range of nanoscale morphologies controlled by the volume fractions of each block (f_A and $f_B = 1 - f_A$) and the segregation strength (χN , where χ is the Flory-Huggins interaction parameter and N is the overall degree of polymerization of the polymer) of the BCP chain [9]. At high values of χN , the repulsion between blocks is sufficiently strong to drive self-assembly into ordered nanoscale morphologies, including lamellae, cylinders, spheres, and network phases. However, for low values of χN , where the repulsion between blocks is insufficient, the structure is disordered. This order-disorder transition (ODT) is marked by the segregation strength $\chi N|^{ODT}$. For BCP nanolithography, lamellar and cylindrical morphologies have been studied extensively for templating nanosized lines and posts, respectively. While the features observed are largely controlled by the influence of f_A (or equivalently f_B) on the BCP's packing parameter that dictates the structures that can be formed [10], the characteristic feature sizes result from the interplay between the lengths of the BCPs and the interactions between blocks. For lamellar morphologies in the strong segregation regime ($\chi N \gg \chi N|^{ODT}$), the interlamellar domain spacing (d) was predicted by Semenov [11–13] to follow the scaling relationship

$$d = \beta \chi^{1/6} N^{2/3}, \quad (1)$$

where β is a constant. While this expression suggests the domain spacings can be reduced by lowering χ or

Published by the American Physical Society under the terms of the Creative Commons Attribution 4.0 International license. Further distribution of this work must maintain attribution to the author(s) and the published article's title, journal citation, and DOI.

N , χ is determined by the chemical composition of the BCP, limiting its utility in controlling the structural sizes. While N is a viable control parameter, the range of domain sizes available is limited by the condition $\chi N > \chi N|^{ODT}$ for self-assembly. Selection of high- χ BCPs enables the use of low N to achieve smaller features. For example, poly(styrene-*b*-dimethylsiloxane) has a significantly larger χ (~ 0.26) than the industry standard poly(styrene-*b*-methylmethacrylate) with χ (~ 0.06) [14]. Another strategy for controlling feature dimensions is the use of alternate chain architectures [15].

Poelma *et al.* [16] reported that the lamellar domain spacing of cyclic block copolymers is nearly half of that of analogous (equal molecular weight) linear block copolymers. The synthesis of cyclic BCPs, however, is challenging, frequently yielding a blend of linear and cyclic polymers in the final product. Nevertheless, we have previously demonstrated that the domain spacing of linear–cyclic BCP blends is not significantly impacted when linear chains constitute less than 10% of the mixture [17]. With respect to the ODT of pure cyclic BCP systems, theory [18–20], simulation [21,22], and experiments [23,24] have found that the phase diagram of cyclic BCPs is qualitatively similar to that of linear BCPs, but the ODT for symmetric cyclic BCPs is shifted to higher segregation strengths with $\chi N|_{cyc}^{ODT} \approx 1.7 \times \chi N|_{lin}^{ODT}$. Thus, it is more difficult to get self-assembled nanostructures of cyclic BCPs compared to linear BCPs with the same length N . However, Poelma *et al.* [16] showed that when cyclic and linear BCPs of similar molecular size are compared (a cyclic BCP of length N compared to a linear BCP of length $N/2$), the cyclic BCP self-assembled under conditions where the linear BCP was disordered. Thus, we asked whether blending a disordered linear BCP with an ordered cyclic BCP could be a potential route to smaller features. Because blending BCPs either homotopologically (linear polymers with linear polymers) or heterotopologically (linear polymers with cyclic polymers) is not well explored, we approached our study systematically, covering a range of polymer chain lengths and blend compositions.

Experimental [25] and theoretical [26] studies of linear–linear BCP blends have examined their miscibility criterion based on the relative molecular weights of the constituent chains, but comparatively little attention has been focused on blend ODTs. An experimental study [16] on blends of poly(styrene-*b*-isoprene) BCPs found that the blend components were miscible and formed single-period lamellae if their molecular weight ratios (large polymer to short polymer) were smaller than about 5, but the blend components phase separated into coexisting long- and short-period lamellae for a molecular weight ratio of about 10. This result was later reproduced by a self-consistent field theory study [26]. Floudas *et al.* [27] also studied linear–linear blends of poly(styrene-*b*-isoprene) copolymers in the miscible regime but in the vicinity of the ODT. They reported that these blends behaved like a single-component system with a number-average degree of polymerization equal to the mean blend degree of polymerization.

In this work, we use dissipative particle dynamics (DPD) to computationally investigate the ODT in BCP blends. DPD has been used extensively to study the features of classical

morphologies in diblock [28–32], triblock [33,34], multi-block [35–38], multiarm [39], and cyclic [21] copolymers, as well as for visualizing expected morphologies for several chemically specific diblock [40–44] copolymer systems. In simulations containing cyclic BCPs, we note that the unphysical bond crossing permitted in DPD simulation may lead to knotted and concatenated conformations for cyclic chains. Although the impact of disallowing bond crossing on cyclic polymer conformation in the melt state has been seen in some simulations of linear–cyclic homopolymer blends when chains are much longer than those simulated in our work [45], others have shown that for sufficiently short chains, cyclic polymers exhibit Gaussian scaling, and bond crossing has negligible impact on conformational statistics [46–50]. Supporting this assumption, Huang *et al.* [51] showed that decreasing the frequency of unphysical bond crossings (by enhancing the spring–spring repulsion) has negligible effect on resulting equilibrium phase behavior and nanofeature size. Likewise, our previous DPD simulation results on domain spacing for pure cyclic BCPs [17] and for blends of linear and cyclic BCPs [15], as well as results presented in this paper, are in good agreement with theory and experiment, suggesting that bond crossing has negligible impact on the self-assembled equilibrium structures and the feature sizes.

In the present study, we examine the impact of molecular weight disparity between constituent BCPs on the ODT of heterotopological blends (linear + cyclic BCPs) and homotopological blends (linear + linear BCPs). The molecular weights of linear and cyclic BCPs in the blends are chosen independently, and χ is varied systematically to determine the blend ODTs. We characterize the system structure using RDFs (radial distribution functions) and the microphase separation of blend components using cluster analysis.

II. MATERIALS AND METHODS

We performed DPD simulations as described in the Supplemental Material [52] (see Sec. I; see also Refs. [53–56]). For this study, DPD simulations were performed using the LAMMPS software package [57]. The cubic simulation box had a size of $30 \times 30 \times 30$ (DPD length units, with one unit equal to the radius of a single DPD monomer) with 81 000 DPD monomers, resulting in a bead number density of $\rho = 81\,000/30^3 = 3$. The temperature was fixed at 1 in DPD units. Similarly, the mass and radius of each bead was fixed at 1 in DPD units. The interaction parameter (with the dimension of energy per length) between like beads, a_{AA} and a_{BB} , was fixed to 25 (in DPD units) in all simulations, while the cross interaction between unlike beads, a_{AB} , was varied systematically to moderate the repulsion between *A* and *B* blocks. These interaction parameters were mapped to the Flory-Huggins χ parameter as [56]

$$\chi = \frac{1}{3.27} (a_{AB} - a_{AA}). \quad (2)$$

The velocity-Verlet [58] algorithm was used to integrate the equations of motion with a time step of $\Delta t = 0.025$ in DPD units. All the simulations were equilibrated for at least 10^6 time steps, followed by a production run of 5×10^5

time steps for evaluation of thermodynamic averages. At least 50 configurations evenly sampled from production runs were used for data analysis. Error analysis was performed using Jackknife resampling [59]. All simulations were performed on the Ashbaugh group's Dell cluster. Initial configurations for the blends were generated randomly. Since the volume fractions of A and B blocks are equal in all cases (i.e., $f_A = 0.5$), all blends form lamellae above the ODT. For convenience, we refer to cyc- A_mB_n as $C2m$ and lin- A_nB_n as $L2n$, where $2m$ and $2n$ are the degrees of polymerization of cyclic and linear BCP chains, respectively. For example, cyc- $A_{18}B_{18}$ is shortened as $C36$, and we follow this nomenclature in the rest of the paper. The cyclic-linear blends studied are $C8/L16$, $C10/L18$, $C16/L16$, $C12/L12$, $C24/L12$, $C16/L8$, $C24/L8$, $C32/L8$, and $C36/L6$ and are chosen such that there is a greater disparity between the molecular weights of the components in blends like $C8/L16$ and $C36/L6$. The blend compositions varied from $\varphi_{\text{cyc}} = 0$ to 1 in increments of $\Delta\varphi_{\text{cyc}} = 0.1$. In addition to the cyclic-linear BCP blends, we also studied linear-linear BCP blends of $L6/L18$ and $L12/L16$ with compositions ranging from φ_{L6} (or φ_{L12}) = 0 to 1 in increments of $\Delta\varphi_{L6}$ (or $\Delta\varphi_{L12}$) = 0.1. As N , the degree of polymerization, is not well defined for blends of dissimilar molecular weight components, for two-component blend, (1 and 2), we define \tilde{N} (the mean "degree of polymerization of a blend") as

$$\tilde{N} = \varphi_1 N_1 + \varphi_2 N_2, \quad (3)$$

where φ_i is the volume fraction with $\varphi_1 + \varphi_2 = 1$, and N_i is the degree of polymerization of the respective component. For example, a $C36/L6$ blend at $\varphi_{C36} = 0.3$ would have $\tilde{N} = 0.3(36) + 0.7(6) = 15$.

A. Identification of the ODT

Benchmark simulations were run both in series, i.e., the configuration of a prior simulation was the starting point for the next one, and in parallel, i.e., multiple simulations at different a_{AB} were run from the same starting configuration to detect the ODTs. Series simulations were run both forward (increasing a_{AB}) and backward (decreasing a_{AB}). All methods yielded the same $\chi\tilde{N}|^{\text{ODT}}$ with a relative error of 3% or less, which is negligibly small (see Fig. S1 in the Supplemental Material [52]). Most of the blends were simulated in parallel for the study. A cross-interaction increment of $\Delta a_{AB} = 0.25$ was used for the ODT runs. We estimate $\chi\tilde{N}|^{\text{ODT}}$ as the average of $\chi\tilde{N}|_{-}^{\text{ODT}}$ (where the subscript “-” indicates the simulated value of $\chi\tilde{N}$ just below the ODT) and $\chi\tilde{N}|_{+}^{\text{ODT}}$ (where the subscript “+” indicates the simulated value of $\chi\tilde{N}$ just above the ODT). The ODT is a weakly first-order transition for linear [60] and cyclic [61] BCPs of finite molecular weights while the transition is second order in the limit of infinite molecular weights [62]. Thus, the blends studied here are expected to show a jump in total internal energy (a consequence of a first-order transition) across the ODT although the jump is not anticipated to be large. Since part of the total energy is the result of contacts among unlike beads (repulsive energy), and the system tends to reduce such undesired contacts upon ordering, a discontinuous drop in such contacts is also expected across the ODT. Also, the lamellar phase is more orientationally ordered than the disordered

phase. We exploit these features along with visual inspection of system configurations to identify the ODT. The calculation procedures for determining the number of undesired contacts and the chain-orientation order parameter are described below.

Two unlike beads are identified as being in contact with each other if the distance between them is less than the cutoff value of 1 in DPD units and the beads are part of different chains. The reason for choosing the distance cutoff of 1 is that the nonbonded repulsive potential of DPD is zero beyond 1, meaning that the beads lying beyond the cutoff distance do not interact with the reference bead. We count only the interchain A/B bead contacts because the ODT is driven by minimization of the interfacial contact area between the two domains, which in turn reduces the system's free energy [9]. We normalize the mean interchain A/B bead contacts by dividing by the total number of beads in the simulation box and denote it by $\langle n_{AB} \rangle$. A discontinuous drop in $\langle n_{AB} \rangle$ is a signature of the ODT.

Far from the ODT in the disordered phase, the chains orient randomly, and the system is isotropic. As χN approaches $\chi N|^{\text{ODT}}$ the chains start aligning, and their alignments become stronger at higher segregation strength. To quantify the change in alignment, we calculate an orientational order parameter and use it to distinguish between a disordered phase and an ordered lamellar phase. The calculation procedure is as follows: For each chain, we find the center of mass (COM) of the A block and the COM of the B block. The vector starting from A -COM and ending at B -COM gives the orientation of the chain. Next, we translate this vector so that it originates from the origin. The director for this set of chain-orientation vectors is the eigenvector that spans the largest variance, and it describes the preferential orientation of the chains in the simulation box. For the lamellar phase, the director is normal to the lamellar plane. We calculate the orientational order parameter $\langle P_2 \rangle$, the mean of the second Legendre polynomial describing the chain orientation, according to

$$\langle P_2 \rangle = \frac{1}{2}(3\langle \cos^2\theta \rangle - 1), \quad (4)$$

where θ is the angle between the chain-orientation vector and the director. In our simulations, a value of $\langle P_2 \rangle$ approaching 1 indicates a strongly aligned, ordered lamellar phase and the value approaching zero indicates a random distribution of chain orientations characteristic of a disordered phase. While mathematically negative values of $\langle P_2 \rangle$ are possible, this result would correspond to chain alignment normal to the director (or in-plane alignment of chains within a lamella), which is physically unreasonable for our system.

B. Cluster analysis

To investigate the segregation of blend components in the disordered phase near the ODT, we perform cluster analysis on the A beads in the simulation box using the following algorithm: Starting from a reference A bead on a cyclic chain, the adjacent A bead is deemed to be part of the same cluster as the reference bead if it belongs to the same chain or lies on another cyclic chain and is within a distance cutoff of 1 in DPD units. This process is repeated until all A beads on cyclic chains have been considered. This process is repeated for the A beads of the linear BCP component. The number average mean cluster size for component i of the blend normalized by

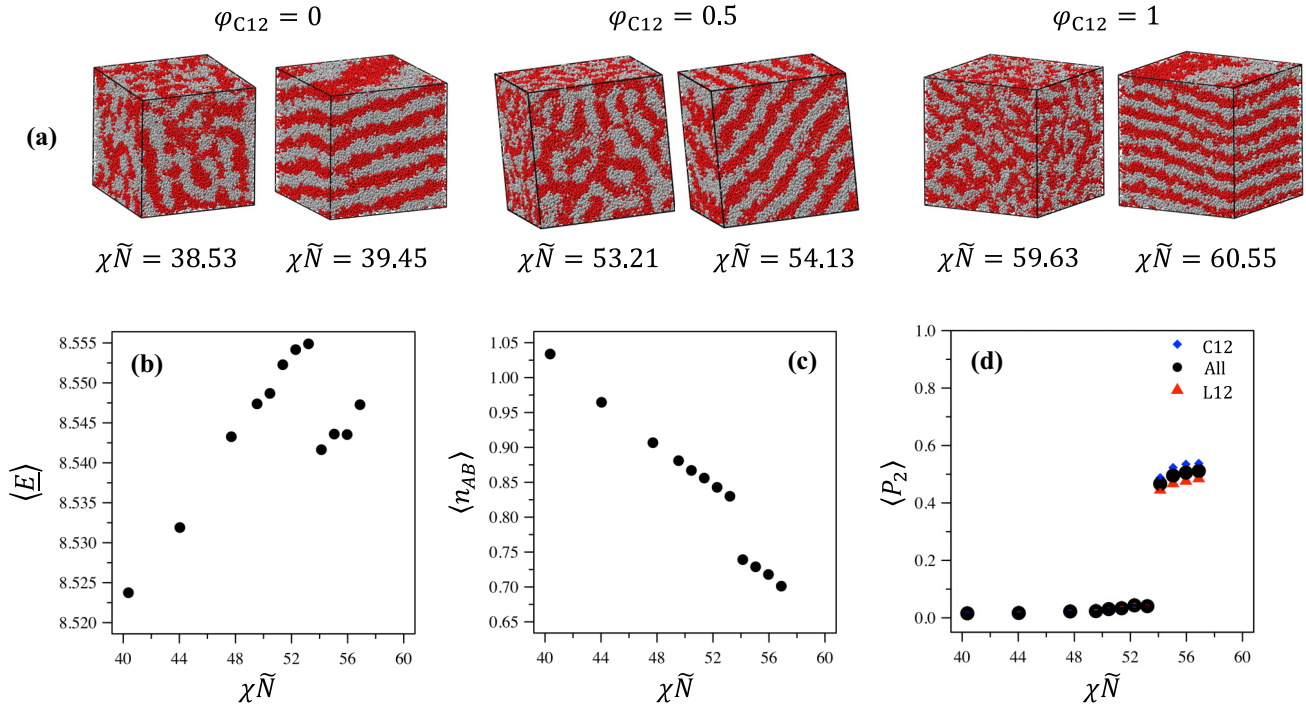


FIG. 1. Methods to detect the order-disorder transition. (a) Simulation snapshots rendered by VMD [65] at $\chi\tilde{N}|_{-}^{\text{ODT}}$ (just below the ODT), and at $\chi\tilde{N}|_{+}^{\text{ODT}}$ (just above the ODT) for pure L12 (first figure), pure C12 (last figure), and 50% C12/L12 blend (middle figure). The gray and red regions consist of *A* and *B* blocks, respectively. Variation of the (b) mean total internal energy per bead, $\langle E \rangle$ (c) mean interchain *A/B* bead contacts per bead, $\langle n_{AB} \rangle$; and (d) orientational order parameter, $\langle P_2 \rangle$, with $\chi\tilde{N}$ in 50% blend. Error bars are smaller than figure symbols. The ODT is characterized by the jumps exhibited in the three preceding methods and consistent with the simulation snapshots.

the total number of *A* beads belonging to component *i* in the simulation box, $\langle n_c/n \rangle_i$, is calculated according to

$$\left\langle \frac{n_c}{n} \right\rangle_i = \frac{\sum_j [n_{j,i} \cdot \left(\frac{n_{j,i}}{n_i} \right)]}{n_i}, \quad (5)$$

where $n_{j,i}$ is the number of *A* beads belonging to cluster *j* and component *i*, and n_i is the total number of *A* beads belonging to component *i* in the simulation box. A normalized cluster size close to zero indicates the presence of many small clusters of a few beads, whereas a value approaching 1 indicates almost all the beads are connected forming a single, simulation-box spanning cluster.

III. RESULTS AND DISCUSSION

A. Order-disorder transition

Figure 1(a) shows simulation snapshots of L12 (lin- A_6B_6), C12 (cyc- A_6B_6), and a 50 vol% blend of the two polymers at $\chi\tilde{N}|_{-}^{\text{ODT}}$ (just below the ODT) and at $\chi\tilde{N}|_{+}^{\text{ODT}}$ (just above the ODT) of each system. Below the ODT, the *A* and *B* blocks are segregated, but the system adopts a disordered bicontinuous structure akin to a sponge [63]. Just above the ODT, on the other hand, the *A* and *B* blocks segregate into an ordered lamellar structure. While this transition is apparent visually, the ODT is also evident from changes in thermodynamic and structural quantities. Figures 1(b)–1(d) show the mean internal energy per bead, $\langle E \rangle$, mean number of *A/B* contacts per bead, $\langle n_{AB} \rangle$, and the orientational order parameter $\langle P_2 \rangle$ as a function of $\chi\tilde{N}$ for the 50 vol % L12/C12 blend. Each of these

variables changes discontinuously between $\chi\tilde{N}$ of 53.21 and 54.13 suggesting the ODT occurs between these two values, in agreement with visual examination of the simulation snapshots. In the case of the energy [Fig. 1(b)], a marked drop is observed in the energy across the ODT, partly as a result of the drop in *A/B* contacts observed in Fig. 1(c). Indeed, Beardsley and Matsen [64] demonstrated that the ODT is linked to a discontinuous drop in $\langle n_{AB} \rangle$. In the case of the chain-orientational order parameter, below the ODT $\langle P_2 \rangle$ is nearly zero, indicative of no orientational order. Above the ODT, $\langle P_2 \rangle$ discontinuously jumps from approximately 0 to 0.5, indicative of orientational reordering of the chains into lamellar structures. Indeed, the increase in $\langle P_2 \rangle$ suggests the polymers adopt a mean angle of $\sim 35^\circ$ (or $\sim 145^\circ$ for polymers oriented in the opposite direction) with respect to the lamellar normal. Taken together, these observations support the proposition that the ODT can be reliably determined from both thermodynamic and structural variables obtained from our simulations. Nevertheless, the precise location of the ODT is not determined directly, but rather is bounded by $\chi\tilde{N}|_{-}^{\text{ODT}}$ and $\chi\tilde{N}|_{+}^{\text{ODT}}$ determined from simulation. We estimate $\chi\tilde{N}|^{\text{ODT}}$ as the average of these values (i.e., $\chi\tilde{N}|^{\text{ODT}} = (\chi\tilde{N}|_{-}^{\text{ODT}} + \chi\tilde{N}|_{+}^{\text{ODT}})/2$, which is $53.67 = (53.21 + 54.13)/2$ for the 50% vol % C12/L12 blend illustrated in Fig. 1).

In Fig. 2(a) we show $\chi\tilde{N}|^{\text{ODT}}$ for C36/L6 blends as a function of φ_{C36} , the volume fraction of the cyclic component. First, as expected, $\chi\tilde{N}|_{C36}^{\text{ODT}}/\chi\tilde{N}|_{L6}^{\text{ODT}} = 64/39 \approx 1.6$ is in reasonable agreement with the theoretical prediction of 1.7 and with previous simulation studies [21]. Second,

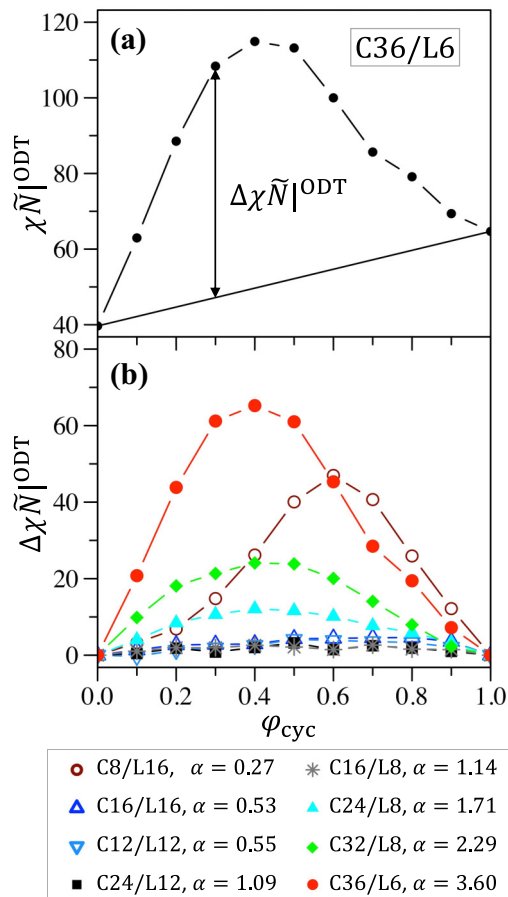


FIG. 2. (a) A graphical representation of the definition of $\Delta\chi\tilde{N}|^{\text{ODT}}$. The solid circles are calculated $\chi\tilde{N}|^{\text{ODT}}$ for C36/L6 blends at various compositions. The broken lines between the circles are drawn for guidance. The solid line connecting $\chi\tilde{N}|^{\text{ODT}}$ at $\varphi_{\text{C36}} = 0$ and $\chi\tilde{N}|^{\text{ODT}}$ at $\varphi_{\text{C36}} = 1$ is obtained by the linear interpolation between the pure-component values of $\chi\tilde{N}|^{\text{ODT}}$. The vertical line with double arrows represents the $\Delta\chi\tilde{N}|^{\text{ODT}}$ for a blend with $\varphi_{\text{C36}} = 0.3$. (b) Variation of $\Delta\chi\tilde{N}|^{\text{ODT}}$ for different blends with volume fraction of cyclic component of the blend (φ_{cyc}). The broken lines drawn are for guidance. All plot symbols are defined in the legend.

and more strikingly, $\chi\tilde{N}|^{\text{ODT}}$ varies nonmonotonically as a function of the blend composition, exhibiting a maximum of 114.9 at $\varphi_{\text{C36}} = 0.4$. That is, it is significantly more difficult to order the blend than the pure BCPs. We note that the absolute values of $\chi\tilde{N}|^{\text{ODT}}$ that we report are based on Eqs. (2) and (3) without any additional corrections to χ , e.g., accounting for finite chain-length effects. Although applying such corrections to our data following methods reported by Gavrilov *et al.* [66] leads to better agreement between our values and others reported in the literature for pure linear BCPs (see Sec. 1 in the Supplemental Material [52]), applying this correction to cyclic BCPs and blends is not straightforward, so we have opted not to do so for consistency within this work.

The simplest expectation for the dependence of $\chi\tilde{N}|^{\text{ODT}}$ on the blend composition would be a linear dependence on φ . We quantify deviations from this expectation in a two-component

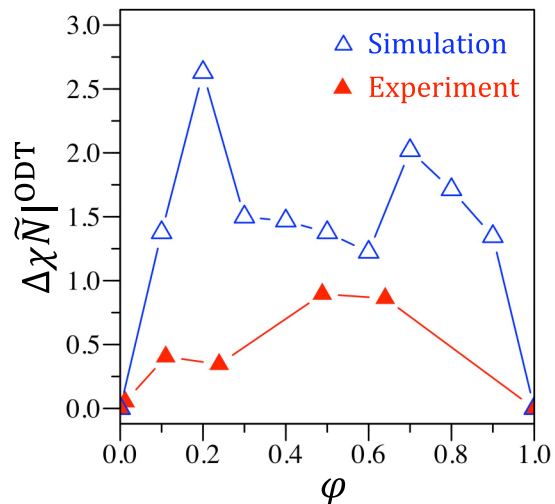


FIG. 3. The comparison of $\Delta\chi\tilde{N}|^{\text{ODT}}$ obtained from an experimental system of linear-linear blends of poly(styrene-*b*-isoprene) [27] with $\alpha = 1.35$ and simulated blends of L12/L16 with similar size mismatch ($\alpha = 1.36$).

blend (1 and 2) by the difference

$$\Delta\chi\tilde{N}|^{\text{ODT}} = \chi\tilde{N}|^{\text{ODT}} - [\varphi_1 \chi N|_1^{\text{ODT}} + \varphi_2 \chi N|_2^{\text{ODT}}], \quad (6)$$

where $\chi\tilde{N}|^{\text{ODT}}$ is the observed ODT for the blend and $\Delta\chi\tilde{N}|^{\text{ODT}}$ is the excess [Fig. 2(a)]. In Fig. 2(b) we report $\Delta\chi\tilde{N}|^{\text{ODT}}$ for a number of blends of linear and cyclic polymers. We generally observe a positive excess over simple mixing for all blends. Moreover, the magnitude of the effect depends on the disparity between the degrees of polymerization of the blended polymers. To quantify this disparity, we define the polymer size mismatch as

$$\alpha = \lambda_1/\lambda_2, \quad (7)$$

where λ_i is the number of bonds in polymer i divided by the number of bonds between unlike monomers in polymer i . This definition is based on our previous work modeling the dimensions of lamellar and hexagonal structures assembled from blended linear and cyclic BCPs [67]. For linear and cyclic polymers, we have

$$\lambda_{\text{lin}} = N_{\text{lin}} - 1 \quad (8a)$$

and

$$\lambda_{\text{cyc}} = N_{\text{cyc}}/2, \quad (8b)$$

where N_i is the degree of polymerization of polymer i . As a convention in this study, for linear-cyclic blends, in Eq. (7) we identify $\lambda_1 = \lambda_{\text{cyc}}$ and $\lambda_2 = \lambda_{\text{lin}}$. In the case of linear-linear polymer blends the identification of λ_1 and λ_2 is arbitrary because α and $1/\alpha$ are equivalent to each other for homotopological blends.

The results in Fig. 2(b) suggest that the magnitude of $\Delta\chi\tilde{N}|^{\text{ODT}}$ is strongly correlated with α . Specifically, for α values close to 1 (no size mismatch) $\Delta\chi\tilde{N}|^{\text{ODT}}$ is nearly zero, indicative of ideally blended polymers. When the α is large, however, $\Delta\chi\tilde{N}|^{\text{ODT}}$ exhibits large positive deviations from ideal blending. For homotopological BCP blends (e.g., blends of two linear or two cyclic polymers), $\Delta\chi\tilde{N}|^{\text{ODT}}$ is the same

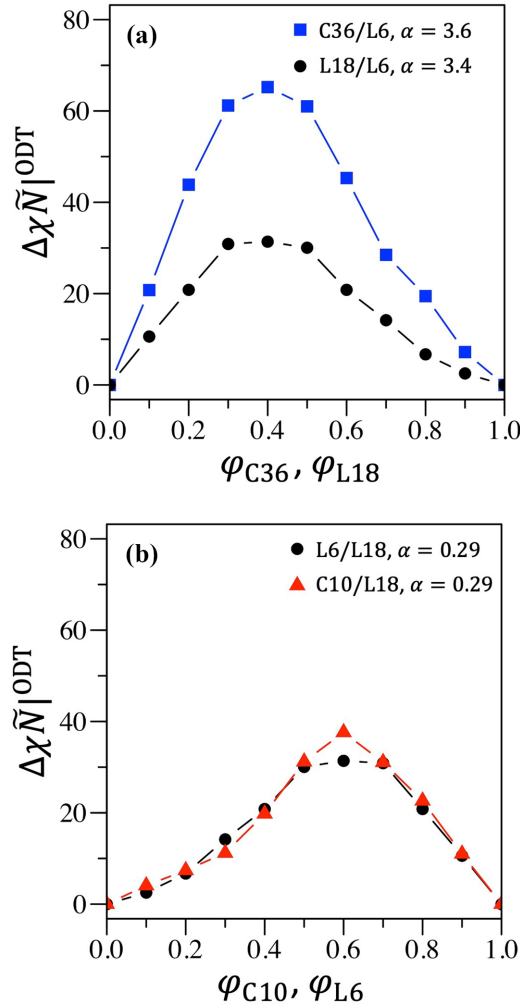


FIG. 4. Impact of topology on $\Delta\chi\tilde{N}|_{\text{ODT}}$. Comparison between the variations of $\Delta\chi\tilde{N}|_{\text{ODT}}$ for (a) C36/L6 and L18/L6 blends with the volume fraction of its larger component, respectively, and (b) L6/L18 and C10/L18 blends with the volume fraction of its smaller component, respectively. All plot symbols are explained in the legends. The broken lines drawn are for guidance.

for polymer mismatches of α and $1/\alpha$ due to the symmetry of the two polymers. For heterotopological blends this symmetry is broken, and this expectation fails. For example, in Fig. 2(b) we find that the maximum of the C36/L6 blend ($\alpha = 3.6$) is more than 50% that of the C8/L16 ($\alpha = 0.27 \approx 1/3.6 = 0.28$) blends. These observations suggest that both the contour length mismatch and topological differences impact the onset of order within the polymer blend.

We subsequently asked (i) whether this effect could have arisen from the finite size of the simulation box (i.e., could macrophase separation into coexisting lamellar or lamellar + disordered phases be the true equilibrium state for some blends, particularly those with high $\Delta\chi\tilde{N}|_{\text{ODT}}$), and (ii) whether it has been observed experimentally. To address the question of macrophase separation, we ran additional simulations of C36/L6 blends at $\varphi_{\text{C36}} = 0.4$ from a starting configuration in which linear and cyclic chains were separated in the simulation box (see Fig. S2 in the Supplemental Material [52]). These simulations always resulted in a single phase

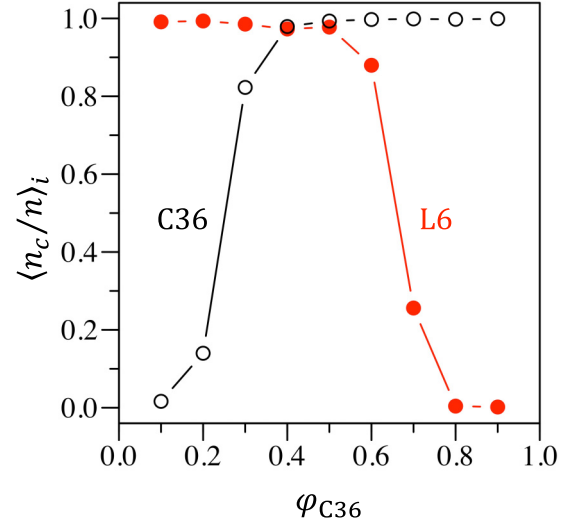


FIG. 5. Self-aggregation behavior of components in C36/L6 blends. The hollow black circles and red solid circles represent the variation of normalized cluster size of the cyclic and the linear components of the blends, respectively, with the volume fraction of the cyclic component in the blend, φ_{C36} . Both components form simulation-box spanning clusters ($\langle n_c/n \rangle_i > 0.8$) at intermediate volume fractions ($0.3 \lesssim \varphi_{\text{C36}} \lesssim 0.6$) in the blend. Outside this window, the minority component is dispersed into smaller clusters. Error bars are smaller than figure symbols.

(either a mixed disordered phase or single-period lamellae) with no hint of macrophase separation, suggesting that the increase in blend $\Delta\chi\tilde{N}|_{\text{ODT}}$ we see is an indication of a physical phenomenon, not an artifact of the simulation method. With respect to comparing to experiment, little research has been conducted on linear–cyclic blends; however, Floudas *et al.* [27] have reported experimental results for linear–linear poly(styrene-*b*-isoprene) blends with $\alpha = 1.35$ (Fig. 3; see Sec. 2 in the Supplemental Material [52] for procedure used to obtain the experimental $\Delta\chi\tilde{N}|_{\text{ODT}}$ from data reported in Floudas *et al.* [27]). From their data, it can be inferred that the blend ODT shows positive deviations from ideal mixing due to the polymer size mismatch, although the deviations are small due to α being close to 1. We compare these experimental results against our simulations for an L16/L12 blend ($\alpha = 1.36$). While we observe greater noise due to the finite differences used to estimate $\Delta\chi\tilde{N}|_{\text{ODT}}$ from simulation, our results are in semiquantitative agreement with the experiment. This comparison lends confidence that the DPD simulations are capturing the physics underlying the impact of blending size-mismatched polymers on the ODT.

To further examine the impact of polymer topology on $\Delta\chi\tilde{N}|_{\text{ODT}}$ we consider homotopological (linear–linear) and heterotopological (linear–cyclic) blends with comparable values of α . Specifically, in Fig. 4 we compare results for blends of C36/L6 vs L18/L6 [$\alpha = 3.6$ and 3.4 , respectively; Fig. 4(a)] and C10/L18 vs L6/L18 [$\alpha = 0.29$ for both blends; Fig. 4(b)]. For the C36/L6 and L18/L6 blends [Fig. 4(a)] in which the topology of the larger component differs (C36 vs L18), we observe a more significant impact of topology. Specifically, the magnitude of $\Delta\chi\tilde{N}|_{\text{ODT}}$ over the entire

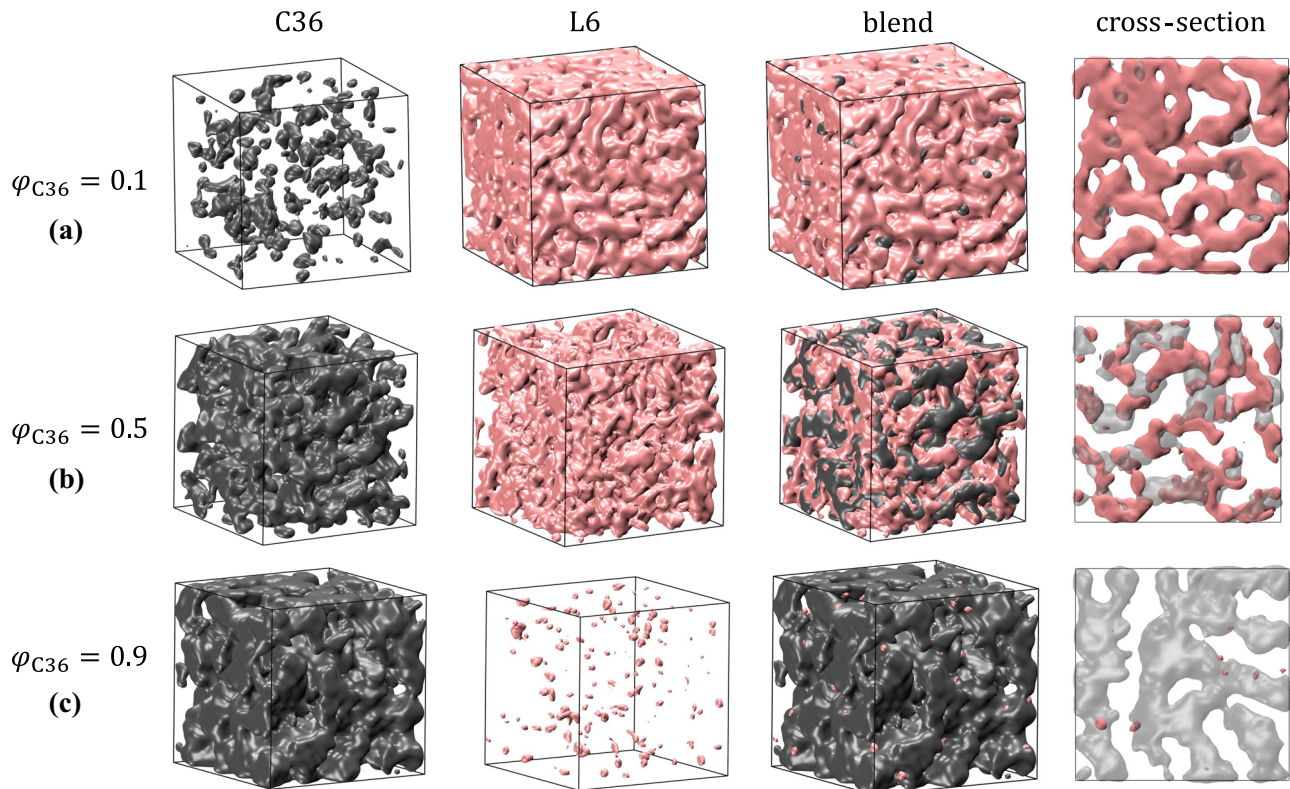


FIG. 6. Simulation snapshots demonstrating the organization of individual components in C36/L6 blends at three different blend compositions at their respective $\chi\tilde{N}|_{\text{ODT}}$. First two columns show the individual blend components, third represents the blend, and last column shows a top view of a cross section of the simulation box. (a) At $\varphi_{\text{C36}} = 0.1$, cyclic chains are dispersed as disconnected clusters in the blend while the linear chains form a single simulation-box spanning cluster. (b) At intermediate composition ($\varphi_{\text{C36}} = 0.5$), both components form simulation-box spanning clusters individually. (c) At $\varphi_{\text{C36}} = 0.9$, linear chains are dispersed as disconnected clusters in the blend while the cyclic chains form a single simulation-box spanning cluster. Only *A* beads are shown in all the figures for clarity.

concentration range for the heterotopological blend is more than twice that of the homotopological blend. In contrast, for the C10/L18 and L6/L18 blends [Fig. 4(b)] in which the topology of the smaller component differs (C10 vs L6), we find $\Delta\chi\tilde{N}|_{\text{ODT}}$ for the two blends are effectively the same. We subsequently surmise that the differences in the magnitudes of $\Delta\chi\tilde{N}|_{\text{ODT}}$ between hetero- and homotopological blends are exacerbated by the topology of the larger component of the blend. This difference is made even greater the larger the size mismatch between the blend components.

B. Chain organization in the disordered phase

To gain insight into the positive deviations of $\Delta\chi\tilde{N}|_{\text{ODT}}$ from ideal mixing, we consider the properties of blends C36/L6 ($\alpha = 3.6$), C24/L12 ($\alpha = 1.09$), and C8/L16 ($\alpha = 0.27$) at $\chi\tilde{N}|_{\text{ODT}}$, just below their ODTs. We perform cluster analysis on the *A* beads in the simulation box (see Sec. II, Materials and Methods) to examine the self-aggregation of blend constituents (e.g., clustering of L6 with L6 and C36 with C36). Figure 5 reports the normalized mean cluster sizes ($\langle n_c/n \rangle_i$) of C36 and L6 as a function of φ_{C36} at $\chi\tilde{N}|_{\text{ODT}}$. For $\varphi_{\text{C36}} > 0.3$, the majority of the cyclic polymer chains belong to a simulation-box spanning cluster of cyclic chains ($\langle n_c/n \rangle_i > 0.8$). On the other hand, a greater concentration of the linear component (L6) is required to meet this

self-aggregation threshold, occurring for $\varphi_{\text{L6}} \gtrsim 0.4$ ($\varphi_{\text{C36}} = 1 - \varphi_{\text{L6}} \lesssim 0.6$). For intermediate compositions ($0.3 \lesssim \varphi_{\text{C36}} \lesssim 0.6$), both the linear and cyclic components form simulation-box spanning aggregates. We note that the greatest values of $\Delta\chi\tilde{N}|_{\text{ODT}}$ also occur in this composition range. Outside this window, the minority component is dispersed into smaller clusters and individual chains. Qualitatively similar conclusions can be drawn from blends of C24/L18 and C8/L16 (see Figs. S3 and S5 in the Supplemental Material [52]).

The aggregation behavior inferred from our cluster analysis is confirmed visually by considering simulation snapshots in Fig. 6 at distinct concentrations of the C36/L6 blend (see Figs. S4 and S6 in the Supplemental Material for similar snapshots for the C24/L12 and C8/L16 blends [52]). The first and second columns of Fig. 6 represent clusters of C36 and L6 alone, respectively, while the third column shows both clusters together. The last column represents the top view of a cross section of the simulation. The top, middle, and bottom rows in this figure indicate results at blend compositions of $\varphi_{\text{C36}} = 0.1, 0.5$, and 0.9 , respectively, representing the three clustering conditions identified in Fig. 5. As surmised above, for $\varphi_{\text{C36}} = 0.1$ and 0.9 , the minority component, the cyclic polymer for $\varphi_{\text{C36}} = 0.1$ and the linear polymer for $\varphi_{\text{C36}} = 0.9$, exists in smaller clusters dispersed in the majority component, which forms a simulation-box spanning cluster (Fig. 6). For $\varphi_{\text{C36}} = 0.5$, it appears that each blend component preferen-

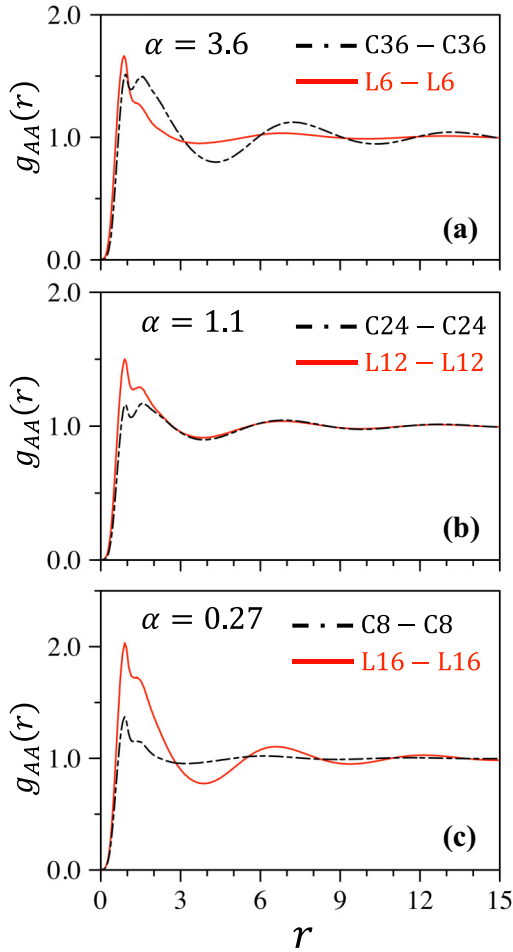


FIG. 7. Interchain radial distribution function among the A beads in the cyclic chain, and A beads in linear chains for blends (a) C36/L6, (b) C24/L12, and (c) C8/L16 at $\varphi_{\text{cyc}} = 0.5$ and their respective $\chi\tilde{N}|_{\text{ODT}}^{\text{ODT}}$ values. For blend C24/L12, the overlap between the RDFs for linear and cyclic chains for most radial distances indicates that the two coexisting structures, formed by linear chains and cyclic chains, are commensurate with each other, while such coexisting structures are more incommensurate in blends with greater size mismatch between their blend components (C36/L6 and C8/L16) alluded by their nonoverlapping RDFs. All plot symbols are defined in the legend.

tially associates with itself to form a simulation-box spanning cluster.

In Fig. 7(a), we report the interchain RDF $g_{AA}(r)$ for C36 and for L6 at $\varphi_{\text{C36}} = 0.5$ at $\chi\tilde{N}|_{\text{ODT}}^{\text{ODT}}$. In turn, $g_{AA}(r)$ is equivalent to $g_{BB}(r)$ by symmetry. We find that the cyclic chains, C36, exhibit significant long-range structure as indicated by the periodic maxima and minima in $g_{AA}(r)$. While the linear chains, L6, also exhibit maxima and minima, the amplitude of these oscillations is considerably weaker than that observed for its cyclic counterpart. This suggests that the structure of the blend at this composition is dominated by the larger cyclic component ($\alpha = 3.6$), while the smaller linear component appears more dispersed. Similar observations can be made for the case of C8/L16 ($\alpha = 0.27 \approx 1/3.6 = 0.28$) blends where again the larger chains, now linear (L16), dominate the structure [Fig. 7(c)]. Furthermore, the positions of the

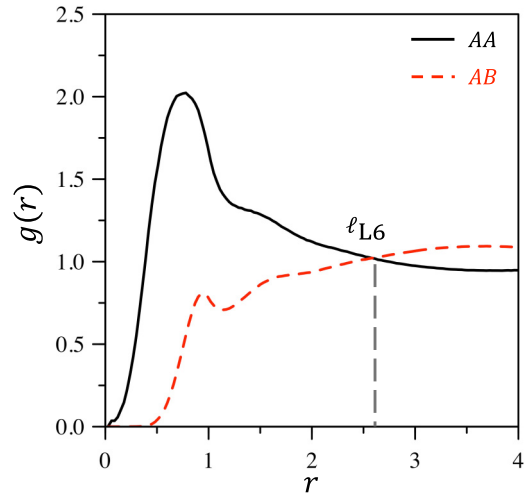


FIG. 8. Method used to quantify the characteristic length associated with the structure formed by the linear chains in the blend at a given $\chi\tilde{N}$. The first crossover between the interbead RDFs calculated between like beads and unlike beads gives an estimate for this length (ℓ_{L6}). All plot symbols are defined in the legend. The system shown here is a C36/L6 blend with $\varphi_{\text{C36}} = 0.4$ at $\chi\tilde{N}|_{\text{ODT}}^{\text{ODT}}$.

maxima and minima for each component $g_{AA}(r)$ are out of phase in the blends with large size mismatch (C36/L6, $\alpha = 3.6$ and C8/L16, $\alpha = 0.27$), whereas the components of a blend with minimal size mismatch (C24/L12, $\alpha = 1.1$), form a harmonious structure, with oscillations coinciding beyond the first peak [Fig. 7(b)]. The offset between the positions of the maxima and minima for blend components indicates the presence of mismatched larger-scale structures formed by the components in the blend.

C. Incommensurability between the coexisting structures

Based on our observations, we hypothesize that the blended polymers form incommensurate structures near the ODT in the disordered phase, disrupting the long-range order within the sample. As a result, higher segregation strengths are needed to reduce this incommensurability and enforce the mesoscale structure of the blend, resulting in positive deviations from ideal mixing in $\chi\tilde{N}|_{\text{ODT}}^{\text{ODT}}$. Here, we quantify the ‘‘incommensurability’’ between the blended polymers in terms of a characteristic length associated with each component domain, denoted as ℓ_i for component i . The value of ℓ_i is taken as the first crossing point of interbead $g_{AA}(r)$ and $g_{AB}(r)$ for that component. The calculation of the characteristic lengths associated with linear polymer domains for a C36/L6 blend is illustrated in Fig. 8. We evaluated the characteristic lengths of C36 domains and L6 domains at varying values of $\chi\tilde{N}$, above and below the ODT, across the composition range $0.1 \leq \varphi_{\text{C36}} \leq 0.7$.

Taking the ratio of blend-component characteristic lengths as a measure of size mismatch, we plot these values against $\chi\tilde{N}$ in Fig. 9. For all compositions, ℓ_{C36} and ℓ_{L6} both increase as $\chi\tilde{N}$ increases due to domain coarsening, but the two components have different dependencies on $\chi\tilde{N}$ such that the ratio $\ell_{\text{C36}}/\ell_{\text{L6}}$ decreases as $\chi\tilde{N}$ increases, with $\chi\tilde{N}|_{\text{ODT}}^{\text{ODT}}$ occurring when $1.25 \gtrsim \ell_{\text{C36}}/\ell_{\text{L6}} \gtrsim 1.1$. This trend is seen for C8/L16

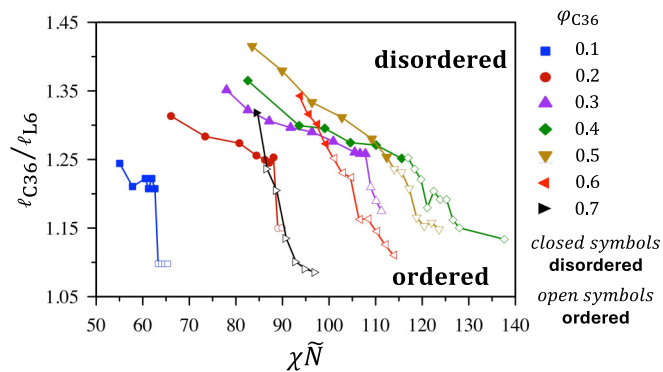


FIG. 9. The ratios of characteristic lengths corresponding to the structures formed by cyclic chains and linear chains in C36/L6 blends plotted with $\chi\tilde{N}$ at compositions between $\varphi_{C36} = 0$ and $\varphi_{C36} = 0.7$. The blends at $\varphi_{C36} = 0.8$ and $\varphi_{C36} = 0.9$ are excluded because at these compositions linear chains do not cluster enough to have meaningful characteristic lengths associated with their structures. All plot symbols are defined in the legend.

and C24/L12 blends as well (see Figs. S7 and S8 in the Supplemental Material [52]), suggesting that increasing commensurability between coexisting structures is necessary for the transition from disorder to order in BCP blends that form single-period lamellae (in contrast to blends that macrophase separate into short- and long-period lamellar phases). We can rationalize the $\Delta\chi\tilde{N}|^{\text{ODT}}$ phenomenon in size-mismatched BCP blends in the following manner: For a single-period lamellar phase to form, both components must conform (or nearly conform) to a single lamellar period that is different from their pure-component lamellar periods. Thus, a driving force greater than that predicted by simple interpolation between the pure-component $\chi N|^{\text{ODT}}$ values is needed to drive phase separation of a blend, giving rise to $\Delta\chi\tilde{N}|^{\text{ODT}}$.

In size-mismatched heterotopological linear-cyclic blends, we see that the magnitude of $\Delta\chi\tilde{N}|^{\text{ODT}}$ depends on which component (linear or cyclic) is larger (Fig. 4). The precise thermodynamic origin of the topological contribution to $\Delta\chi\tilde{N}|^{\text{ODT}}$ is unclear but possibly related to differences in conformational entropy changes of blend components through the disorder to order transition. More specifically, the greater $\Delta\chi\tilde{N}|^{\text{ODT}}$ associated with the C36/L6 blend compared to the L18/L6 and C10/L18 blends, despite having the same size mismatch, implies that a larger enthalpic driving force is needed to promote order in blends containing larger cyclic

BCPs; from this implication, we can infer that larger cyclic BCPs experience greater conformational entropy loss upon ordering than smaller linear or cyclic BCPs. Differences in concentration fluctuations [18] between cyclic and linear BCPs, which have been invoked to explain the difference between pure linear and pure cyclic BCP ODTs ($\chi N|_{\text{cyc}}^{\text{ODT}} \approx 1.7 \times \chi N|_{\text{lin}}^{\text{ODT}}$), may also contribute to the dependence of $\Delta\chi\tilde{N}|^{\text{ODT}}$ on blend composition and size mismatch.

IV. CONCLUSIONS

We systematically studied the order-disorder transition (ODT) in heterotopological block copolymer blends of linear and cyclic BCPs with independently chosen chain lengths ranging from $N = 6$ to $N = 36$. We found that the blend ODT always occurs at a higher segregation strength than one would predict from simple linear interpolation between pure-component $\chi N|^{\text{ODT}}$ values. The magnitude of this deviation, $\Delta\chi\tilde{N}|^{\text{ODT}}$, increases with increasing size mismatch between blend components. Comparison of heterotopological blends (linear-cyclic) to homotopological blends (linear-linear) at the same size mismatch, α , revealed that the $\Delta\chi\tilde{N}|^{\text{ODT}}$ phenomenon depends on both the magnitude of α and the topologies of the blend components. Specifically, $\Delta\chi\tilde{N}|^{\text{ODT}}$ is greater in heterotopological blends with $\alpha > 1$, whereas blends with $\alpha < 1$ exhibit similar values of $\Delta\chi\tilde{N}|^{\text{ODT}}$ as the homotopological linear-linear blend at the same value of α . Upon closer examination of the structures formed just above and just below $\chi\tilde{N}|^{\text{ODT}}$, we found that the blend components self-aggregate in the disordered phase, forming clusters with different characteristic lengths. Ordering is most hindered at intermediate compositions (i.e., around $\varphi = 0.5$), where both components form simulation-box spanning clusters in the disordered phase, and the onset of order only occurs only when sufficient commensurability is achieved between the characteristic lengths associated with these clusters. As blending BCPs is an attractive strategy to manipulate feature sizes for nanolithographic applications, these insights provide helpful guidance and understanding with respect to the impacts of polymer size mismatch and topology on the ordering transition for self-assembly of BCP blends.

ACKNOWLEDGMENT

We gratefully acknowledge support from the National Science Foundation (Grant No. NSF CMMI-1825881) for supporting this research.

- [1] E. M. Gordon, *Proc. SPIE* **2439** (1995).
- [2] M. Neisser, *J. Microelectron. Manuf.* **1**, 1 (2018).
- [3] R. R. Dammel, *J. Photopolym. Sci. Technol.* **24**, 33 (2011).
- [4] Editorial, *Nat. Photonics* **3**, 361 (2009).
- [5] C. M. Bates, M. J. Maher, D. W. Janes, C. J. Ellison, and C. G. Willson, *Macromolecules* **47**, 2 (2014).
- [6] T.-Y. Lo, M. R. Krishnan, K.-Y. Lu, and R.-M. Ho, *Prog. Polym. Sci.* **77**, 19 (2018).
- [7] G. G. Yang, H. J. Choi, K. H. Han, J. H. Kim, C. W. Lee, E. I. Jung, H. M. Jin, and S. O. Kim, *ACS Appl. Mater. Interfaces* **14**, 12011 (2022).
- [8] E. R. Gottlieb, A. Guliyeva, and T. H. Epps, III, *ACS Appl. Polym. Mater.* **3**, 4288 (2021).
- [9] F. S. Bates, *Science* **251**, 898 (1991).
- [10] *Intermolecular and Surface Forces*, 3rd ed., edited by N. I. Jacob (Academic Press, Boston, 2011), pp. 503.
- [11] A. N. Semenov, *Macromolecules* **26**, 6617 (1993).
- [12] A. E. Likhtman and A. N. Semenov, *Europhys. Lett.* **51**, 307 (2000).
- [13] A. N. Semenov, *Zh. Eksp. Teor. Fiz.* **88**, 1242 (1985).
- [14] D. Borah, R. Senthamaraiannan, S. Rasappa, B. Kosmala, J. D. Holmes, and M. A. Morris, *ACS Nano* **7**, 6583 (2013).

- [15] A. D. Goodson, M. S. Rick, J. E. Troxler, H. S. Ashbaugh, and J. N. L. Albert, *ACS Appl. Polym. Mater.* **4**, 327 (2022).
- [16] J. E. Poelma, K. Ono, D. Miyajima, T. Aida, K. Satoh, and C. J. Hawker, *ACS Nano* **6**, 10845 (2012).
- [17] A. D. Goodson, J. E. Troxler, M. S. Rick, H. S. Ashbaugh, and J. N. L. Albert, *Macromolecules* **52**, 9389 (2019).
- [18] J. F. Marko, *Macromolecules* **26**, 1442 (1993).
- [19] G. Zhang, Z. Fan, Y. Yang, and F. Qiu, *J. Chem. Phys.* **135**, 174902 (2011).
- [20] J. U. Kim, Y.-B. Yang, and W. B. Lee, *Macromolecules* **45**, 3263 (2012).
- [21] H.-J. Qian, Z.-Y. Lu, L.-J. Chen, Z.-S. Li, and C.-C. Sun, *Macromolecules* **38**, 1395 (2005).
- [22] T. Herschberg, J.-M. Y. Carrillo, B. G. Sumpter, E. Panagiotou, and R. Kumar, *Macromolecules* **54**, 7492 (2021).
- [23] A. Takano, O. Kadoi, K. Hirahara, S. Kawahara, Y. Isono, J. Suzuki, and Y. Matsushita, *Macromolecules* **36**, 3045 (2003).
- [24] A. K. Khandpur, S. Foerster, F. S. Bates, I. W. Hamley, A. J. Ryan, W. Bras, K. Almdal, and K. Mortensen, *Macromolecules* **28**, 8796 (1995).
- [25] T. Hashimoto, K. Yamasaki, S. Koizumi, and H. Hasegawa, *Macromolecules* **26**, 2895 (1993).
- [26] M. W. Matsen, *J. Chem. Phys.* **103**, 3268 (1995).
- [27] G. Floudas, D. Vlassopoulos, M. Pitsikalis, N. Hadjichristidis, and M. Stamm, *J. Chem. Phys.* **104**, 2083 (1996).
- [28] R. D. Groot and T. J. Madden, *J. Chem. Phys.* **108**, 8713 (1998).
- [29] R. D. Groot, T. J. Madden, and D. J. Tildesley, *J. Chem. Phys.* **110**, 9739 (1999).
- [30] L.-J. Chen, Z.-Y. Lu, H.-J. Qian, Z.-S. Li, and C.-C. Sun, *J. Chem. Phys.* **122**, 104907 (2005).
- [31] F. J. Martínez-Veracoechea and F. A. Escobedo, *J. Chem. Phys.* **125**, 104907 (2006).
- [32] A. R. Khokhlov and P. G. Khalatur, *Chem. Phys. Lett.* **461**, 58 (2008).
- [33] X. Li, I. V. Pivkin, H. Liang, and G. E. Karniadakis, *Macromolecules* **42**, 3195 (2009).
- [34] H. Chen and E. Ruckenstein, *Soft Matter* **8**, 1327 (2012).
- [35] T. Klymko, V. Markov, A. Subbotin, and G. T. Brinke, *Soft Matter* **5**, 98 (2009).
- [36] C.-I. Huang, C.-H. Liao, and T. P. Lodge, *Soft Matter* **7**, 5638 (2011).
- [37] A. A. Gavrillov, Y. V. Kudryavtsev, P. G. Khalatur, and A. V. Chertovich, *Chem. Phys. Lett.* **503**, 277 (2011).
- [38] H. Tan, Z. Wang, J. Li, Z. Pan, M. Ding, and Q. Fu, *ACS Macro Lett.* **2**, 146 (2013).
- [39] Y. Wang, B. Li, Y. Zhou, Z. Lu, and D. Yan, *Soft Matter* **9**, 3293 (2013).
- [40] W.-J. Lee, S.-P. Ju, Y.-C. Wang, and J.-G. Chang, *J. Chem. Phys.* **127**, 064902 (2007).
- [41] V. Ortiz, S. O. Nielsen, D. E. Discher, M. L. Klein, R. Lipowsky, and J. Shillcock, *J. Phys. Chem. B* **109**, 17708 (2005).
- [42] C. Soto-Figueroa, M.-d.-R. Rodríguez-Hidalgo, J.-M. Martínez-Magadán, and L. Vicente, *Macromolecules* **41**, 3297 (2008).
- [43] S. Roy, D. Markova, A. Kumar, M. Klapper, and F. Müller-Plathe, *Macromolecules* **42**, 841 (2009).
- [44] X. Li, J. Guo, Y. Liu, and H. Liang, *J. Chem. Phys.* **130**, 074908 (2009).
- [45] K. Hagita, T. Murashima, H. Shiba, N. Iwaoka, and T. Kawakatsu, *Comput. Mater. Sci.* **203**, 111104 (2022).
- [46] M. E. Cates and J. M. Deutsch, *J. Phys.* **47**, 2121 (1986).
- [47] M. Müller, J. P. Wittmer, and M. E. Cates, *Phys. Rev. E* **53**, 5063 (1996).
- [48] D. Richter, S. Gooßen, and A. Wischniewski, *Soft Matter* **11**, 8535 (2015).
- [49] J. D. Halverson, G. S. Grest, A. Y. Grosberg, and K. Kremer, *Phys. Rev. Lett.* **108**, 038301 (2012).
- [50] M. Kruteva, J. Allgaier, and D. Richter, *Macromolecules* **56**, 4835 (2023).
- [51] C. I. Huang, L. F. Yang, C. H. Lin, and H. T. Yu, *Macromol. Theory Simul.* **17**, 198 (2008).
- [52] See Supplemental Material at <http://link.aps.org/supplemental/10.1103/PhysRevMaterials.8.045603> for Dissipative particle dynamics formalism; Procedure to obtain the experimental $\Delta\chi N|^{ODT}$; Data for C8/L16 and C24/L12 blends; References associated with Supplemental Material.
- [53] P. J. Hoogerbrugge and J. M. V. A. Koelman, *Europhys. Lett.* **19**, 155 (1992).
- [54] J. M. V. A. Koelman and P. J. Hoogerbrugge, *Europhys. Lett.* **21**, 363 (1993).
- [55] P. Español and P. Warren, *Europhys. Lett.* **30**, 191 (1995).
- [56] R. D. Groot and P. B. Warren, *J. Chem. Phys.* **107**, 4423 (1997).
- [57] S. Plimpton, *J. Comput. Phys.* **117**, 1 (1995).
- [58] M. P. Allen and D. J. Tildesley, *Computer Simulation of Liquids* (Oxford University Press, Oxford, 2017).
- [59] B. Efron and C. Stein, *Ann. Stat.* **9**, 586 (1981).
- [60] G. H. Fredrickson and E. Helfand, *J. Chem. Phys.* **87**, 697 (1987).
- [61] W. H. Jo and S. S. Jang, *J. Chem. Phys.* **111**, 1712 (1999).
- [62] L. Leibler, *Macromolecules* **13**, 1602 (1980).
- [63] T. Vidil, N. Hampu, and M. A. Hillmyer, *ACS Cent. Sci.* **3**, 1114 (2017).
- [64] T. M. Beardsley and M. W. Matsen, *Eur. Phys. J. E* **32**, 255 (2010).
- [65] W. Humphrey, A. Dalke, and K. Schulten, *J. Mol. Graphics* **14**, 33 (1996).
- [66] A. A. Gavrillov, Y. V. Kudryavtsev, and A. V. Chertovich, *J. Chem. Phys.* **139**, 224901 (2013).
- [67] A. D. Goodson, G. Liu, M. S. Rick, A. W. Raymond, M. F. Uddin, H. S. Ashbaugh, and J. N. L. Albert, *J. Polym. Sci. Part B: Polym. Phys.* **57**, 794 (2019).